Processing and Application of Ceramics 12 [4] (2018) 374–382
https://doi.org/10.2298/PAC1804374T

BY-NC-ND

Mesoporous TiO_2 spheres as a photoanodic material in dye-sensitized solar cells

Nikola Tasić[1,*], Zorica Marinković Stanojević[1], Zorica Branković[1], Milan Žunić[1], Uroš Lačnjevac[1], Martina Gilić[2], Tatjana Novaković[3], Goran Branković[1]

[1]*Institute for Multidisciplinary Research, Department of Materials Science, University of Belgrade, Kneza Višeslava 1, 11030 Belgrade, Serbia*
[2]*Institute of Physics Belgrade, University of Belgrade, Pregrevica 118, 11080 Belgrade, Serbia*
[3]*IChTM-Department of Catalysis and Chemical Engineering, University of Belgrade, Njegoševa 12, 11000 Belgrade, Serbia*

Received 22 June 2018; Received in revised form 15 October 2018; Accepted 27 November 2018

Abstract

Mesoporous TiO_2 films with spherical architectures and promising performance in dye-sensitized solar cells (DSSCs) were prepared. The morphology of the films was investigated by scanning electron microscopy. Transmission electron microscopy analysis of the spheres disclosed the elongated shape of sub-20 nm primary particles, while BET analysis revealed their high surface area of 135 m^2/g. Anatase presence was observed in the films based on X-ray diffractometry, selected-area electron diffraction analysis and Raman spectroscopy analyses. Increased light scattering of the spheres in visible region was observed by UV-VIS-NIR spectroscopy. Photovoltaic performance of the operating N719-sensitized cells was tested using electrochemical impedance spectroscopy and current density-voltage (J-V) curves under simulated AM1.5 spectrum. The 0.25 cm^2 cells exhibited photo-to-electric power efficiency of 4.9%, which is among noteworthy values for DSSCs with similar photoanodic structures.

Keywords: *dye-sensitized solar cells (DSSCs), TiO_2, photoanode, mesoporous spheres*

I. Introduction

Dye-sensitized solar cells (DSSCs) have emerged as cost-effective alternative to the conventional *p-n* junction photovoltaic devices, ever since their discovery by Grätzel and O'Regan [1]. Experimentally confirmed advantages of DSSCs over *p-n* junction cells include simple fabrication process, functionality over wide range of temperatures, relative insensitivity of the conversion efficiency towards the angle of incident light, low weight and flexibility [2]. The main component of these cells is the photoactive anode, typically made of porous TiO_2 film, covered with the monolayer of light harvesting dye [3]. Several types of dyes have been used over the years, including Ru(II)- [4], Os(II)- and Fe(II)-polypyridyl complexes [5,6], d^{10}-Cu(I) complexes [7], porphyrins [8] and organosilicon compounds [9]. On the other hand, numerous TiO_2 porous anodic structures have been proposed, such as uniform monolith films [10,11] or complexed architectures consisting of nanospheres [12], nanotubes [13], nanorods [14] or nanowires [15]. The idea behind the utilization of complexed architectures is to promote the light scattering within the sensitized film, and consequently increase the operating parameters of DSSCs, i.e. open-circuit voltage (V_{OC}) and/or short-circuit current density (J_{SC}). Such structures, apart from hierarchical (micro, meso) porosity which allows unobstructed distribution of dye and electrolyte, should also possess high surface area, which enables higher uptake of the light-harvesting component.

This paper, as a continuation of our work in the field of dye-sensitized solar cells, focuses on the photovoltaic performance of three-dimensional spherical photoanode prepared using modification of our previously reported fabrication procedure [11]. The primary nanosized particles of the proposed structure are essentially the same as previously presented, however, the processing route,

* Corresponding authors: tel: +381 11 2085059,
e-mail: *nikola.tasic@imsi.bg.ac.rs*

leading to the fabrication of films and the morphology of the films, are completely different. The spheres were synthesized using hydrothermally-assisted sol-gel method, then mixed with the appropriate organic functional agents to form doctor blade paste and processed into films to serve as the photoanodic support for N719-dye in the operating cell. We present thorough electrochemical characterization of the proposed device in order to explain the charge transfer processes and determine the photovoltaic parameters of merit, and compare the obtained data with literature values for uniform structure consisting of the same core material [11] and similar three-dimensional structures.

II. Experimental procedure

2.1. Synthesis of microspheres and film preparation

Sub-micronic micelles consisting of nanoanatase particles were synthesized using method from our previous study [11]. The objective of this study was to preserve the obtained hierarchical structure throughout the processing of the hydrothermally-synthesized micelles into photoanodic films. Titanium(IV)-isopropoxide (TTIP, Alfa Aesar, 97% min.) was dissolved in isopropanol (i-PA, VWR), and then non-ionic surfactant Triton X100 (TX100, J.T. Baker) was dropwise added to the solution to form viscous precursor solution, with respect to the molar ratio of TTIP : TX100 : i-PA = 1 : 1 : 40. Then, the capping agent EDTA-Na_2 (Aldrich Chemistry), using molar ratio of TTIP : EDTA-Na_2 = 4 : 1, was added at a slow pace into the stirring mixture with the transfer pipette. Afterwards, the peptization process was promoted and completed by heating the reaction mixture for 3 h at 80 °C. The formed precipitate was dissolved in 20 ml of distilled H_2O, and transferred into the stainless steel autoclave for hydrothermal treatment (Carl Roth, Model II, high-pressure autoclave) at 200 °C for 18 h, under autogeneous pressure.

Doctor blade paste was prepared by the addition of α-terpineol (95% min., Alfa Aesar) and ethyl-cellulose (viscosity 4 cP, Aldrich Chemistry), into the product of hydrothermal synthesis, followed by the weak ultrasound homogenization at 7 W for 3 min (Bandelin Sonoplus 2070HD). The optimized composition of the doctor blade paste was as follows: ethanol rinsed and centrifuged product of hydrothermal synthesis (approx. 1.6 g), α-terpineol (2.25 ml, Alfa Aesar), ethyl-cellulose (0.25 g, Aldrich Chemistry).

The films were deposited onto fluorine-doped tin oxide substrates (FTO, MTI Crystal, 6–8Ω/sq) with the green sheet thickness of ~50 μm. FTO transparent conductive substrates were chosen due to their stability at the calcination temperature which was afterwards applied for the complete degradation of organic paste components. The films were cured at room temperature for 15 min and then dried and calcined on the hot plate (IKA® C-MAG), with the concluding step at 500 °C for 10 min. During the calcination, the films gradually developed milky white colour. Cooled films were immersed in a 50 mM aqueous solution of $TiCl_4$ (Aldrich Chemistry), and thermally treated at 80 °C for 45 min, followed by another drying and calcination treatment. The $TiCl_4$ treatment was performed in order to increase photocurrent density of the operating cell, as previously reported in the literature [16].

2.2. DSSC assembly

The $TiCl_4$-treated films were then cooled to 70 °C and immersed in 0.5 mM solution of cis-bis (isothiocyanato)bis(2,2'-bipyridyl-4,4'-dicarboxylato)-ruthenium(II)bis-tetrabutylammonium (Solaronix, N719) ethanol solution for 24 h. The counter-electrode was prepared by doctor blade deposition of Pt paste (Platisol T/SP, Solaronix) onto FTO glass (MTI Crystal, 12–14 Ω/sq) and calcined at 450 °C for 15 min in the tube furnace (heating rate 5 °C/min). The dye-covered electrode and Pt counter electrode were assembled into a sandwich-type cell and sealed with the binder clips. Finally, the assembled cell was filled with the electrolyte containing the I^-/I^{3-} redox system (Iodolyte 50, Solaronix).

2.3. Characterization of TiO_2 films and DSSCs

The morphology of as prepared films was characterized using scanning electron microscopy (SEM, VEGA3 TESCAN), field-emission scanning electron microscopy (FESEM, MIRA3 TESCAN) and transmission electron microscopy (TEM, JEM-2100 JEOL). The crystallographic structure of the films was investigated on Rigaku RINT 2000 diffractometer with parafocal Bragg-Brentano geometry, using CuKα radiation (λ = 1.54178 Å). Raman spectroscopy of the $TiCl_4$-treated film was performed on Raman 2000 Cromex, equipped with CCD camera and 532 nm Ar laser as the excitation source (power 10 mW). The nitrogen adsorption on the scratched films sample was performed at −196 °C and relative pressure interval between 0.05 and 0.98 in automatic adsorption apparatus (Sorptomatic 1990 Thermo Finningen). Before measurements, samples were degassed at 200 °C under vacuum for the time long enough to observe the absence of significant changes in vacuum stability (4 h < t < 10 h). The adsorbed amount of nitrogen was measured by volume at standard temperature and pressure. The specific surface area S_{BET} was calculated by the BET (Brunauer-Emmett-Teller) method [17–19] from nitrogen adsorption-desorption isotherms, using data up to p/p_0 = 0.3, and the pore size distribution have been computed from desorption branch of the isotherms [19]. The diffuse reflectance and transmittance spectra of the films were recorded using a UV-2600 Shimadzu spectrophotometer with the integrated sphere (medium step measurements).

Both current-voltage (J-V) and electrochemical impedance spectroscopy (EIS) measurements were performed using a Gamry Reference 600 potentiostat. Current-voltage characteristics were acquired at a

sweep rate of 100 mV/s in a voltage range of 0–1.0 V. EIS curves were recorded at a voltage of 0.75 V under illumination (open circuit voltage) and in the dark by applying AC amplitude of 10 mV RMS over a frequency range from 200 kHz to 40 mHz with 20 points per decade. For the illumination purposes we have used an Osram 120 V/300 W ELH halogen lamp at 100 mW/cm, calibrated with Volcraft PL-110SM photometer to simulate AM1.5 spectrum. Complex nonlinear least-squares (CNLS) fitting of an appropriate equivalent circuit to the EIS data was performed by Gamry Echem Analyst software, version 6.25. All equivalent circuit parameters are normalized with respect to the geometric surface area of the working and counter electrode (0.25 cm^2).

III. Results and discussion

3.1. Microstructure of TiO_2 films

The morphology of as prepared TiO_2 films was comprehensively investigated and the related images and data are presented in Fig. 1. Low magnification SEM images of the film surface before and after the $TiCl_4$-treatment (Figs 1a. and 1b.) reveal uniform structure composed of sub-micronic spheres, well interconnected into continuous porous network including nanosized surface cracks (<300 nm in width). No significant changes of the films morphology after the treatment were observed, which is in accordance with the literature findings [16]. Additionally, spheres' size distribution histogram, based on the size analysis performed on the morphology image using precise software tools (SemAfore 5.21) was shown in inset of Fig. 1b. The obtained histogram shows the dominating spheres diameter values in the range of 0.6–1.2 μm. The thickness of the $TiCl_4$-treated film was also determined by SEM analysis of the film's cross-section and it was found to be ~3 μm (Fig. 1c).

The spheres were closely observed using FE-SEM technique and the recorded image presented in Fig. 2a unveils the shape and dimensions of hydrothermally-grown and further calcined primary particles. The nanosized particles are elongated, up to 20 nm in length and less than 10 nm in width, and the uniformity of their shape and dimensions was additionally confirmed by TEM analysis, performed on the scratched film sample (Fig 2b). The particle shape derives from the mutual cooperation between the capping agent EDTA-Na_2 and surfactant Triton X100, during the autoclaving under autogeneous pressure (~10 bar). The presence of EDTA-Na_2 affects the growth of particles, governing their elongated shape, while Triton X100 directs the formation of soft spherical structure [11].

Several studies have been conducted to elucidate the potential benefits of similar three-dimensional assemblies and their dimensions to the performance in DSSCs as the scattering layer [20–22] or the main photoanodic layer [23–25]. Lv *et al.* [20] have shown that even the partially covering scattering layer consisting of non-dispersive solid spheres, sized in the range of 0.6–2 μm, enhances the diffuse reflectance of the photoanode, leading to the increase of photo-to-current efficiency from 4.3 to 5.2%. Yu *et al.* [21] have es-

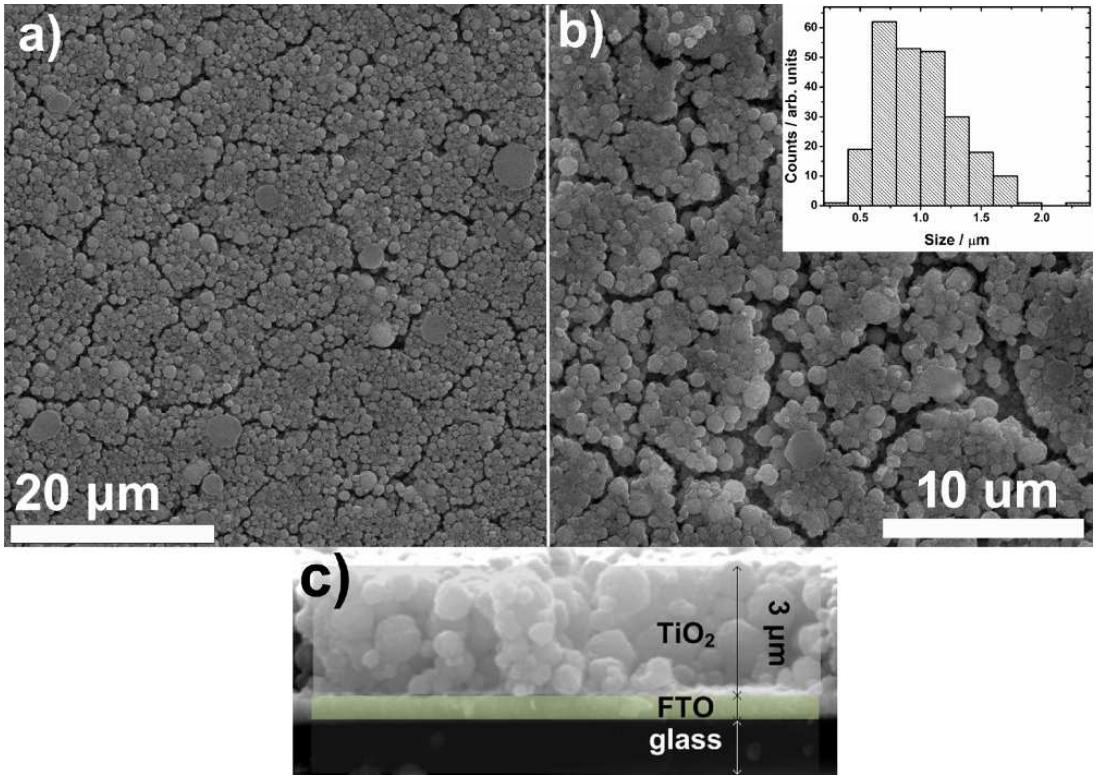

Figure 1. SEM images of: a) the TiO_2 morphology prior to the $TiCl_4$ treatment, b) $TiCl_4$-treated TiO_2 film (inset – spheres size distribution) and c) cross-section of the $TiCl_4$-treated TiO_2 film

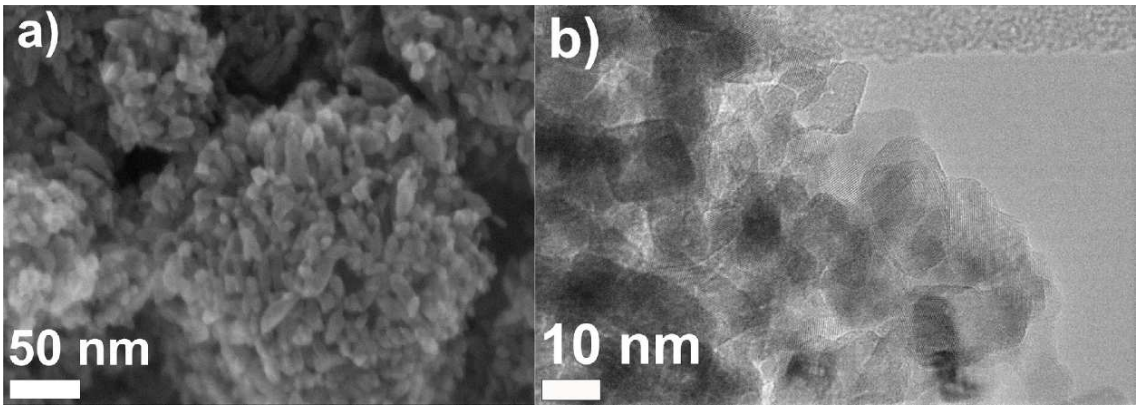

Figure 2. High magnification FE-SEM image of the sub-micronic spheres (a) and primary "rice-like" particles observed by TEM (b)

tablished a dependence between the sphere size and light scattering effects in their systematic study. They showed that 450 nm monodispersed spheres have the best photo-to-current efficiency through the highest increase of reflectance and photocurrent density, compared to 260, 350, 560 or 800 nm spheres. Kim *et al.* [23] have demonstrated that the photoanode consisting of approx. 250 nm uniform spheres has better photovoltaic performance than the uniform photoanode of the same thickness (10 μm), fabricated from the commercially available titania pastes. Finally, Liao *et al.* [24] have shown that even 5 μm hierarchical spheres or approx. 200–400 nm ellipsoidal spheres can perform better as single layer in DSSCs, than randomly oriented 30 nm nanoparticles in uniform layer. Clearly, no strong rule concerning the spheres size and their dispersivity towards the photovoltaic performance can be established. The photovoltaic performance is synthesis-related, and other properties, such as primary particles size, crystallographic structure, internal/external porosity, surface area etc., should also be taken into consideration. Our experimental procedure resulted with the non-dispersive and visibly porous spheres (Fig. 2b), with the diameter distribution, (Fig. 1b) that might show promising photovoltaic performance (due to the enhanced scattering effects) and known advantages of fine primary particles, <20 nm (Fig. 2b).

3.2. Structural characterization of TiO_2 films

Structural characterization of as prepared films was performed using several techniques. By means of XRD analysis (Fig. 3a), it was confirmed that the films calcined at 500 °C consist of the pure anatase phase, with wide diffraction peaks situated at 25.3, 38.0, 48.0, 54.1, 55.0 and 62.8°, corresponding to the following anatase crystallographic planes: (101), (004), (200), (105), (211) and (204), respectively.

The positions and intensities of the peaks are in strong agreement with the anatase JCPDS card No. 21-1272. No other phases were detected, meaning that the chosen calcination temperature and duration of 10 min were insufficient to induce the formation of rutile [26]. The average crystallite size of 11.4 nm was calculated for all reflections of the refined spectrum using Powder Cell 2.4 software (refined cell parameters: a = 3.7909 Å, c = 9.4856 Å). From the perspective of application in DSSCs, photoanodes composing of anatase possess superior behaviour in comparison to photoanodes with other TiO_2 phases [27]. Alternatively, the confirmation of anatase presence was obtained by the means of SAED technique. The corresponding pattern, recorded on the scratched film sample, is shown in Fig. 3b. The pattern was analysed with the appropriate software (Gatan Digital Micrograph 1.70.16) to calculate

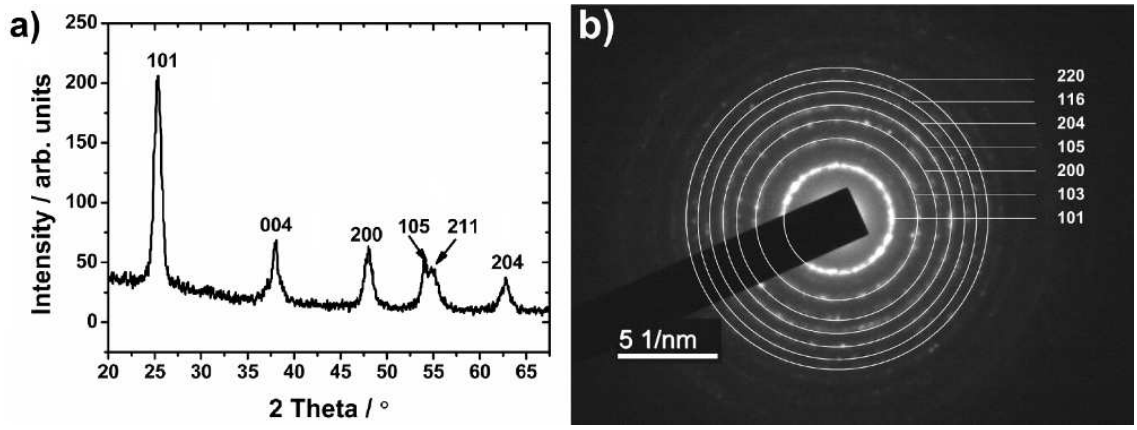

Figure 3. XRD pattern of the film calcined at 500 °C for 10 minutes (a) and SAED pattern of the scratched film sample (b)

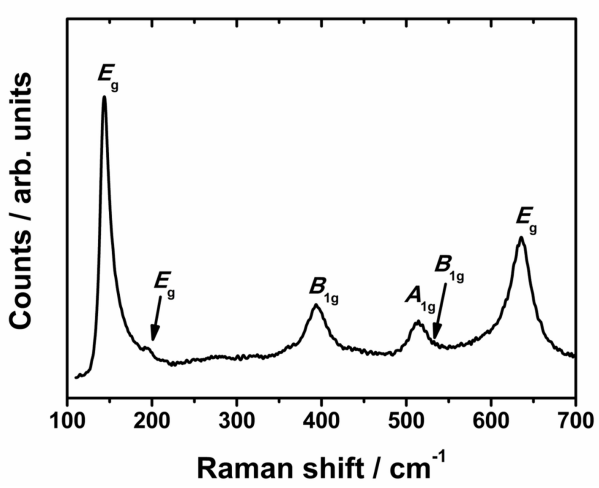

Figure 4. Raman spectrum of the surface modified TiO_2 film

d-spacing values, which completely match the JCPDS card No. 21-1272.

Furthermore, Raman spectroscopy analysis after the modification treatment with $TiCl_4$ (i.e. chemical bath deposition) was performed to investigate the crystallographic nature of the formed surface features. The corresponding spectrum is presented in Fig. 4. Based on the factor group analysis, anatase possesses six Raman active modes ($A_{1g} + 2\,B_{1g} + 3\,E_g$). As shown in Fig. 4, six features are noticeable on the recorded spectrum, and their Raman shift positions are in fair agreement with previously reported data for the anatase crystallographic phase [28].

3.3. BET analysis

In general, good operational properties of DSSCs (short-circuit current density, JSC and photo-to-current efficiency, η) derive from the optimal porosity of photoanodic TiO_2 film, which allows effective distribution of the dye and electrolyte. Furthermore, high specific surface area of TiO_2 particles enables high adsorption of the light-harvesting sensitizer. In a systematic study, Barbe *et al.* [10] have shown that the optimal porosity of TiO_2 films for application in DSSCs is about 70%, while the decrease of average pore size below ~10 nm leads to the non-linear electrolyte diffusion and consequently low photovoltaic response, especially under high illumination.

To determine type of porosity, pore size distribution and the specific surface area, the scratched film sample was subjected to nitrogen adsorption/desorption in automatic adsorption apparatus. Taking into account that the internal porosity and the specific surface area are typically merely affected by the $TiCl_4$-treatment, the measurements were performed only on the non-treated films [16,29]. The sample is characterized with isotherm type IVa, with hysteresis loop of the H1 type (Fig. 5a). Type IVa isotherm is encountered when adsorption occurs on the low porosity material or on the material with predominantly mesoporous pore diameters. The mesoporosity is characterized by the capillary condensation step in the isotherm between relative pressures of 0.5 and 0.8. The sharp steps in the isotherm suggest that capillary condensation occurs in a narrow range of mesopores. On the other hand, hysteresis loop of the H1 type indicates a narrow pore size distribution of uniform pores.

Pore size distribution curve is presented in Fig. 5b, with sharp peaks at ~12.7 and ~14.8 nm, rising from wide background for smaller pores diameter. This means that the mesoporosity within the spheres might not be fully optimal, due to the presence of pores smaller than 10 nm, which typically suffer additional shrinkage after the $TiCl_4$ treatment, due to the more pronounced necks between the primary particles [29]. Finally, the calculated specific surface area of 135 m^2/g is an outstanding feature of the as-synthesized material, nearly 2.5 times larger than for widely utilized commercial powders (such as Degussa P-25) typically used in DSSCs [30].

3.4. Optical properties of TiO_2 films

The role of TiO_2 in DSSCs is reduced to the mechanical support of light-harvesting molecules (and electronic conduction), because TiO_2 alone does not contribute to the utilization of light, owing to its poor

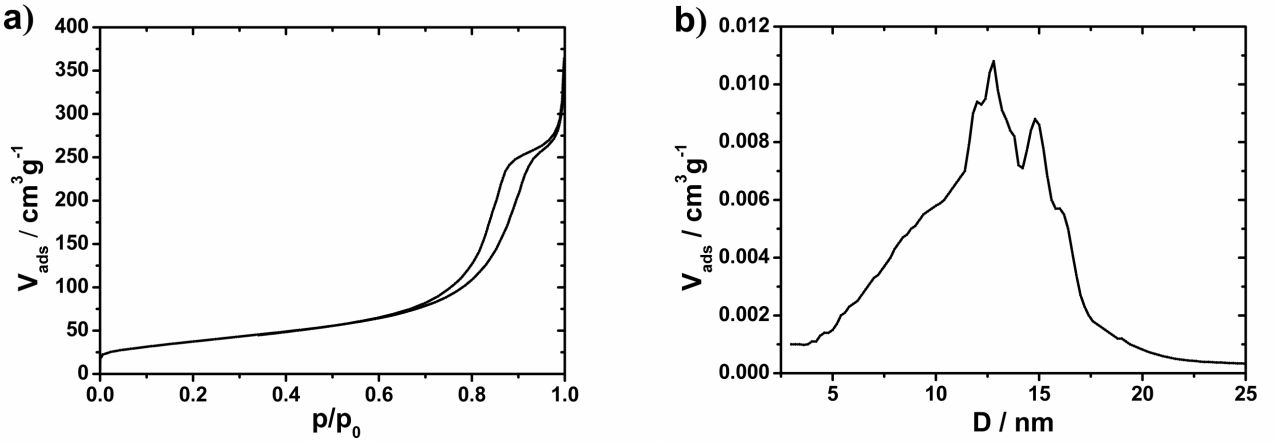

Figure 5. N_2 adsorption-desorption isotherm of TiO_2 film (a) and pore-size distribution curve for TiO_2 film (b)

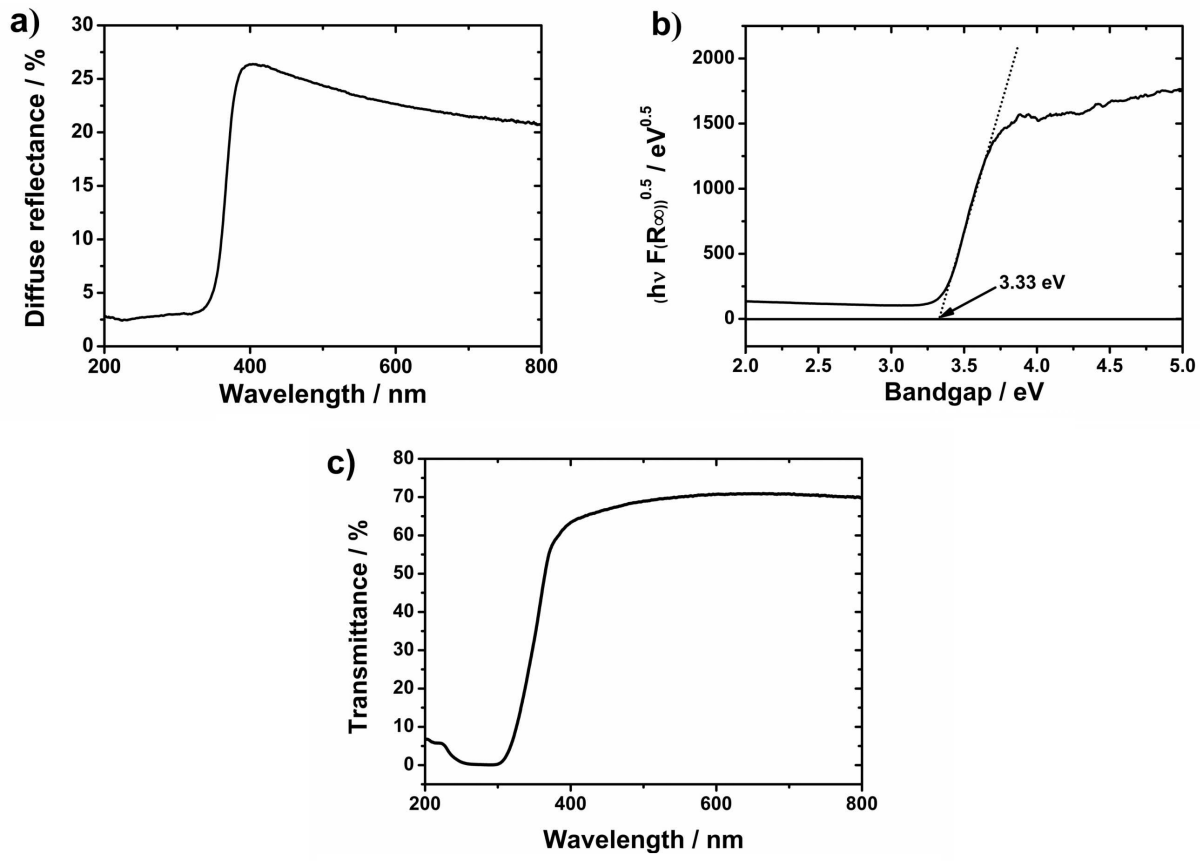

Figure 6. Diffuse reflectance spectrum of prepared TiO_2 film (a), determination of bandgap for TiO_2 film (b) and transmittance spectrum of TiO_2 film (c)

absorption capability (2–3% of Sunlight). However, three-dimensional features with sub-micronic dimensions might promote scattering of the incident light in the cell and enhance the light-harvesting capability of TiO_2 electrodes, without sacrificing the accessible surface for dye loading [12].

Diffuse reflectance spectrum presented in Fig. 6a shows intense visible light (385–785 nm) scattering inside the TiO_2, leading to potentially high photogeneration of electrons. Such behaviour is a direct consequence of the sphere size distribution (Fig. 1c). The recorded spectrum was further transformed using Kubelka-Munk manipulation [31] and Tauc linearization [32] to calculate the indirect bandgap of 3.33 eV (Fig. 6b), which is in fair correspondence to literature value for anatase crystallographic phase of 3.2 eV [33]. Additionally, transmittance percentage in the visible portion of the spectrum is in the range of 63–71% (Fig. 6c).

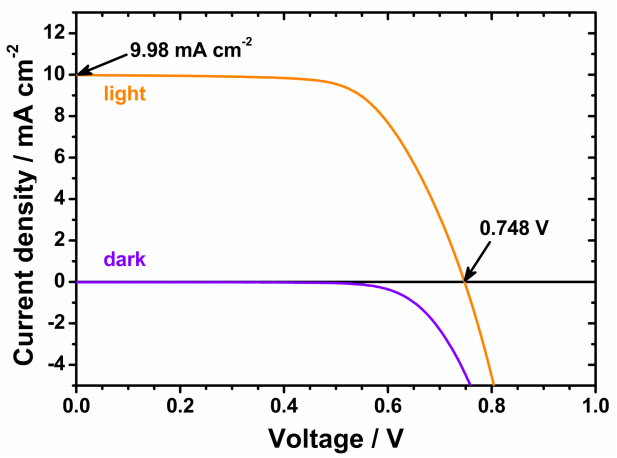

Figure 7. Current density-voltage characteristics of fabricated DSSCs under 100 mW/cm^2 of simulated AM1.5 illumination and under dark conditions

3.5. DSSCs performance

The current-voltage characteristics of the operating DSSC with anatase mesoporous spheres as photoanodic material under illumination and dark conditions are shown in Fig. 7. The photovoltaic parameters of merit, extracted from the curves, are presented in Table 1. The obtained value of 0.75 V for the open-circuit voltage (V_{OC}) is slightly higher than 0.7 V which is typical for anatase-based DSSCs. However, we must emphasize that there are proposed cells in literature with similar spherical structures and substantially lower V_{OC}, as presented in Table 1. Also, the cell exhibits high filling factor (*FF*) of 0.66, which derives from the low thickness of the electrolyte (absence of the spacer between the electrodes), good quality of Pt counter electrode film and the usage of printed silver grids. Despite the presence of the fine pores inside the spheres, and

Table 1. Photovoltaic parameters obtained from current density-voltage curves presented in Fig. 7 together with the referent parameters from other studies

TiO_2 electrode	V_{OC} [V]	J_{SC} [mA/cm^2]	FF	η [%]
This study	0.75	9.98	0.66	4.9
Uniform TiO_2 [11]	0.72	11.336	0.616	5.04
Porous spheres [34]	0.6	15.6	0.53	5.0
P25 + spheres [35]	≤0.606	≤14.9	≤0.625	≤4.82
Hollow spheres [36]	0.732	8.00	0.65	3.79
Hollow spheres [37]	0.64	4.32	0.455	1.26
Microspheres [38]	0.61	5.26	0.67	2.14

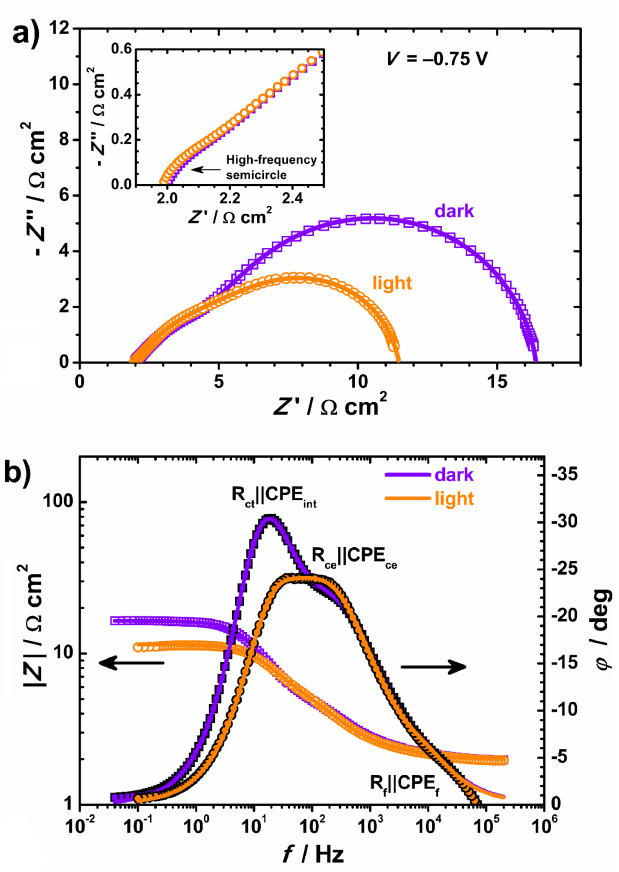

Figure 8. Impedance spectra of the investigated DSSC recorded at VOC conditions, in the dark and under 100 mW/cm^2 illumination, presented using: a) Nyquist plots and b) Bode plots (inset shows a small semicircle observed at high frequencies

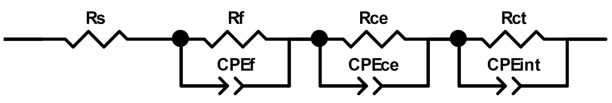

Figure 9. Equivalent circuit used in the CNLS fitting procedure

conceivably low electrolyte diffusion, the cell nearly reached the current-voltage density (J_{SC}) threshold of 10.0 mA/cm^2. Finally, the overall efficiency value of 4.9% is comparable to literature data for similar three-dimensional ordered architectures of porous spheres [34–38], but is still smaller in comparison to the uniform monolith structure [10,11].

3.6. Electrochemical impedance spectroscopy

Electrochemical impedance spectroscopy (EIS) measurements were performed in order to inspect charge transfer/transport processes occurring at interfaces within the device, which are closely related to the DSSC performance and the values of photovoltaic parameters, presented above. Figure 8 shows experimental and simulated Nyquist (a) and Bode plots (b) taken at 0.75 V in the dark and under illumination (V_{OC}). For both conditions the impedance spectra exhibit three partly overlapped semicircles in the Nyquist plot, i.e. three characteristic peaks in the Bode phase plot, which are assigned to the following phenomena: the dielectric behaviour of the TiO_2 film (10^5–10^4 Hz, inset in Fig. 8a) and the charge transfer at the counter electrode/electrolyte (10^4–10^2 Hz) and TiO_2/dye/electrolyte (10^2–10^{-1} Hz) interfaces [11]. The spectra were fitted using a simplified 3CPE model (Fig. 8c) that consists of the equivalent series resistance R_s and three R||CPE circuits connected in series: R_f||CPE$_f$, R_{ce}||CPE$_{ce}$ and R_{ct}||CPE$_{int}$, where R_f represent the TiO_2 film resistance, R_{ct} and R_{ce} are charge transfer resistances at the working and counter electrode interface, respectively, and CPEs are corresponding constant phase elements. Parameters extracted from the fitting procedure are given in Table 2. It can be seen that R_{ct} is halved upon illuminating the cell. Taking into account that R_{ct} reflects the resistance to the electron recombination at the TiO_2 electrode, which mainly proceeds through the reduction of triiodide ions by TiO_2 conduction band electrons, the observed improvement in the reaction kinetics can be correlated with the increase in the local concentration of I^{3-} originating from the regeneration of the photo-excited dye and the ac-

Table 2. Parameters extracted from the CNLS fitting procedure

Condition	R_s [Ω cm^2]	R_f [Ω cm^2]	Y_f [mS s$^\alpha$/cm^2]	α_f	R_{ce} [Ω cm^2]	Y_{ce} [mS s$^\alpha$/cm^2]	α_{ce}	R_{ct} [Ω cm^2]	Y_{int} [mS s$^\alpha$/cm^2]	α_{int}
Dark	2.00	0.109	0.148	1.00	3.48	2.34	0.690	10.8	2.42	0.932
Light	2.00	0.142	0.137	0.995	4.25	2.46	0.698	5.09	3.06	0.940

Table 3. Electron lifetimes and corresponding frequencies, obtained by EIS

Condition	f_{max} [Hz]	τ_{el} [ms]
Dark	7.945	20.0
Light	16.05	9.92

companying oxidation of I^- to I^{3-} [39]. Based on the characteristic frequency corresponding to the R_{ct}||CPE_{int} semicircle maximum, f_{max}, we calculated the average lifetime of the conduction band electrons in the TiO_2 film, τ_{el}, using the equation $\tau_{el} = 1/(2\cdot\pi\cdot f_{max})$. In accordance with the observed R_{ct} trend, the τ_{el} value is found to decrease from 20 ms in the dark to 9.9 ms under light (Table 3). In general, the values of electron lifetime are system dependent and in our case related to the absence of spacer and passivating "recombinations preventing" layer [40] in the cell configuration. Nevertheless, the obtained values of the electron lifetime under illumination are comparable to literature data for the spacer-sealed cells with uniform monolith structure [11,41], high surface area 3D nanoarchitecture [42], or biotemplated hierarchically structured photoelectrodes [43]. Furthermore, we have compared the fitted parameters with the obtained data for uniform monolith photoanode DSSCs from our previous study [11]. We have disclosed correlation between the increase of V_{OC} (0.72 → 0.75 V) and the value of resistance to the electron recombination at the TiO_2 electrode, R_{ct} (17.2 → 20.36 Ω cm^2), confirming that the discrete voltage change might derive from increased recombination resistance and reduced recombination rate [44].

IV. Conclusions

We have prepared photoanodic TiO_2 films containing mesoporous spheres and investigated their application in dye-sensitized solar cells (DSSCs). The films exhibited uniform structure composed of sub-micronic spherical architectures, predominantly 0.6–1.2 μm in size. Systematic microscopy analysis has shown that spheres consisted of sub-20 nm elongated "rice-like" particles. The XRD and SAED of scratched film sample revealed the presence of desirable anatase crystallographic phase, indirectly confirmed by the optical band-gap calculations (3.33 eV). The surface formation of anatase after the $TiCl_4$ treatment was disclosed by the means of Raman spectroscopy. The N_2 adsorption/desorption measurement revealed mesoporosity with non-uniform distribution curve and 135 m^2/g specific surface area. The films were used to fabricate square DSSCs with the area of 0.25 cm^2. The proposed anodic architectures offer higher recombination resistance compared to the uniform monolith structures, leading to the slightly increased value of V_{OC} of the operating device. Furthermore, the obtained solar-to-electric power conversion efficiency of 4.9%, under 100 mW/cm^2 of simulated AM1.5 illumination is comparable to literature data for similar structures.

Acknowledgement: The authors acknowledge the financial support of this paper to the Serbian Ministry of Education, Science and Technological Development through the project No. III45007, and the Bilateral Project between the Republic of Serbia and Republic of Slovenia, under No. 451-03-3095/2014-09-32. The TEM work was conducted in the infrastructure Centre for Electron Microscopy and Microanalysis (CEMM) at Jožef Stefan Institute, Ljubljana (Slovenia).

References

1. B. O'Regan, M. Grätzel, "Low cost and highly efficient solar cells based on the sensitization of colloidal titanium dioxide", *Nature*, **335** (1991) 737–740.
2. R. Jose, V. Thavasi, S. Ramakrishna, "Metal oxides for dye-sensitized solar cells", *J. Am. Ceram. Soc.*, **92** (2009) 289–301.
3. L.M. Gonçalves, V. de Zea Bermudez, H.A. Ribeiro, A.M. Mendes, "Dye-sensitized solar cells: A safe bet for the future", *Energy Environ. Sci.*, **1** (2008) 655–667.
4. M.K. Nazeeruddin, P. Pechy, T. Renouard, S.M. Zakeeruddin, R. Humphry-Baker, P. Comte, P. Liska, P. Cevey, L. Costa, E. Shklover, L. Spiccia, "Engineering of efficient panchromatic sensitizers for nanocrystalline TiO_2-based solar cells", *J. Am. Chem. Soc.*, **123** (2001) 1613–1624.
5. T. Kinoshita, J.I. Fujisawa, J. Nakazaki, S. Uchida, T. Kubo, H. Segawa, "Enhancement of near-IR photoelectric conversion in dye-sensitized solar cells using an osmium sensitizer with strong spin-forbidden transition", *J. Phys. Chem. Lett.*, **3** (2012) 394–398.
6. S. Ferrere, "New photosensitizers based upon $[Fe^{II}(L)_2(CN)_2]$ and $[Fe^{II}L_3]$, where L is substituted 2,2'-bipyridine", *Inorg. Chim. Acta*, **329** (2006) 79–92.
7. T. Bessho, E. Constable, M. Graetzel, A.H. Redondo, C.E. Housecroft, W. Kylberg, M.K. Nazeeruddin, M. Neuburger, S. Schaffner, "An element of surprise-efficient copper-functionalized dye-sensitized solar cells", *Chem. Commun.*, **32** (2008) 3717–3719.
8. A. Yella, H.W. Lee, H.N. Tsao, A.K. Chandiran, M.K. Nazeeruddin, E.W-G. Diau, C-Y. Yeh, S.M. Zakeeruddin, M. Grätzel, "Porphyrin-sensitized solar cells with cobalt(II/III)-based redox electrolyte exceed 12 percent efficiency", *Science*, **334** (2011) 629–634.
9. K. Kakiage, Y. Aoyama, T. Yano, K. Oya, J.I. Fujisawa, M. Hanaya, "Highly-efficient dye-sensitized solar cells with collaborative sensitization by silyl-anchor and carboxy-anchor dyes", *Chem. Commun.*, **88** (2015) 15894–15897.
10. C.J. Barbe, F. Arendse, P. Comte, M. Jirousek, F. Lenzmann, V. Shklover, M. Grätzel, "Nanocrystalline titanium oxide electrodes for photovoltaic applications", *J. Am. Ceram. Soc.*, **80** [12] (1997) 3157–3171.
11. N. Tasić, Z. Marinković Stanojević, Z. Branković, U. Lačnjevac, V. Ribić, M. Žunić, M. Podlogar, G. Branković, "Mesoporous films prepared from synthesized TiO_2 nanoparticles and their application in dye-sensitized solar cells (DSSCs)", *Electrochim. Acta*, **210** (2016) 606–614.
12. D. Chen, F. Huang, Y.B. Cheng, R.A. Caruso, "Mesoporous anatase TiO_2 beads with high surface areas and controllable pore sizes: a superior candidate for high-performance dye-sensitized solar cells", *Adv. Mater.*, **21** (2009) 2206–2210.
13. P. Roy, D. Kim, K. Lee, E. Spiecker, P. Schmuki, "TiO_2

nanotubes and their application in dye-sensitized solar cells", *Nanoscale*, **2** [1] (2010) 45–59.
14. S.H. Kang, S.H. Choi, M.S. Kang, J.Y. Kim, H.S. Kim, T. Hyeon, Y.E. Sung, "Nanorod-based dye-sensitized solar cells with improved charge collection efficiency", *Adv. Mater.*, **20** [1] (2008) 54–58.
15. X. Feng, K. Shankar, O.K. Varghese, M. Paulose, T.J. Latempa, C.A. Grimes, "Vertically aligned single crystal TiO_2 nanowire arrays grown directly on transparent conducting oxide coated glass: synthesis details and applications", *Nano Lett.*, **11** (2008) 3781–3786.
16. P.M. Sommeling, B.C. O'Regan, R.R. Haswell, H.J.P. Smit, N.J. Bakker, J.J.T. Smits, J.M. Kroon, J.A.M. Van Roosmalen, "Influence of a $TiCl_4$ post-treatment on nanocrystalline TiO_2 films in dye-sensitized solar cells", *J. Phys. Chem. B*, **39** (2006) 19191–19197.
17. F. Rouquerol, J. Rouquerol, K.S.W. Sing, P. Llewellyn, G. Maurin, *Adsorption by Powders and Porous Solids, Principles, Methodology and Applications*, Academic Press, New York, 2012.
18. B.C. Lippens, B.G. Linsen, J.H. De Boer, "Studies on pore systems in catalysts I. The adsorption of nitrogen; apparatus and calculation", *J. Catal.*, **3** [1] (1964) 32–37.
19. K.S. Sing, "Reporting physisorption data for gas/solid systems with special reference to the determination of surface area and porosity (Recommendations 1984)", *Pure Appl. Chem.*, **57** [4] (1985) 603–619.
20. F. Lv, S. Xiao, J. Zhu, H. Li, "Dye-sensitized solar cells with enhanced efficiency using hierarchical TiO_2 spheres as a scattering layer", *RSC Adv.*, **68** (2014) 36206–36211.
21. I.G. Yu, Y.J. Kim, H.J. Kim, C. Lee, W. I. Lee, "Size-dependent light-scattering effects of nanoporous TiO_2 spheres in dye-sensitized solar cells", *J. Mater. Chem.*, **21** (2011) 532–538.
22. G. Veerappan, D.W. Jung, J. Kwon, J.M. Choi, N. Heo, G.R. Yi, J.H. Park, "Multi-functionality of macroporous TiO_2 spheres in dye-sensitized and hybrid heterojunction solar cells", *Langmuir*, **11** (2014) 3010–3018.
23. Y.J. Kim, M.H. Lee, H.J. Kim, G. Lim, Y.S. Choi, N.G. Park, W.I. Lee, "Formation of highly efficient dye-sensitized solar cells by hierarchical pore generation with nanoporous TiO_2 spheres", *Adv. Mater.*, **36** (2009) 3668–3673.
24. J.Y. Liao, J.W. He, H. Xu, D.B. Kuang, C.Y. Su, "Effect of TiO_2 morphology on photovoltaic performance of dye-sensitized solar cells: nanoparticles, nanofibers, hierarchical spheres and ellipsoid spheres", *J. Mater. Chem.*, **16** (2012) 7910–7918.
25. M. Ye, C. Chen, M. Lv, D. Zheng, W. Guo, C. Lin, "Facile and effective synthesis of hierarchical TiO_2 spheres for efficient dye-sensitized solar cells", *Nanoscale*, **14** (2013) 6577–6583.
26. D.A. Hanaor, C.C. Sorrell, "Review of the anatase to rutile phase transformation", *J. Mater. Sci.*, **4** (2011) 855–874.
27. N.G. Park, J. Van de Lagemaat, A.J. Frank, "Comparison of dye-sensitized rutile-and anatase-based TiO_2 solar cells", *J. Phys. Chem. B*, **38** (2000) 8989–8994.
28. T. Ohsaka, F. Izumi, Y. Fujiki, "Raman spectrum of anatase, TiO_2", *J. Raman Spectroscop.*, **6** (1978) 321–324.
29. S.W. Lee, K.S. Ahn, K. Zhu, N.R. Neale, A.J. Frank, "Effects of $TiCl_4$ treatment of nanoporous TiO_2 films on morphology, light harvesting, and charge-carrier dynamics in dye-sensitized solar cells", *J. Phys. Chem. C*, **116** (2012) 21285–21290.
30. N. Bowering, G.S. Walker, P.G. Harrison, "Photocatalytic decomposition and reduction reactions of nitric oxide over Degussa P25", *Appl. Catal. B*, **3** (2006) 208–216.
31. P. Kubelka, F. Munk, "An article on optics of paint layers", *Z. Tech. Phys.*, **12** (1931) 593–601.
32. J. Tauc, R. Grigorovici, A. Vancu, "Optical properties and electronic structure of amorphous germanium", *Phys. Status Solidi B*, **15** (1996) 627–637.
33. K.M. Reddy, S.V. Manorama, A.R. Reddy, "Bandgap studies on anatase titanium dioxide nanoparticles", *Mater. Chem. Phys.*, **78** [1] (2003) 239–245.
34. H.E. Wang, L.X. Zheng, C.P. Liu, Y.K. Liu,C.Y. Luan, H. Cheng, Y.Y. Li, L. Martinu, J.A. Zapien, I. Bello, "Rapid microwave synthesis of porous TiO_2 spheres and their applications in dye-sensitized solar cells", *J. Phys. Chem. C*, **115** (2011) 10419–10425.
35. J. Yu, J. Fan, L. Zhao, "Dye-sensitized solar cells based on hollow anatase TiO_2 spheres prepared by self-transformation method", *Electrochim. Acta*, **3** (2010) 597–602.
36. Y. Liu, S. Wang, Z. Shan, X. Li, J. Tian, Y. Mei, H. Ma, K. Zhu, "Anatase TiO_2 hollow spheres with small dimension fabricated via a simple preparation method for dye-sensitized solar cells with an ionic liquid electrolyte", *Electrochim. Acta*, **60** (2012) 422–427.
37. Y. Kondo, H. Yoshikawa, K. Awaga, M. Murayama, T. Mori, K. Sunada, S. Bandow, S. Iijima, "Preparation, photocatalytic activities, and dye-sensitized solar-cell performance of submicron-scale TiO_2 hollow spheres", *Langmuir*, **24** (2008) 547–550.
38. W. Zhang, J. Gu, S. Yao, H. Wang, "The synthesis and application of TiO_2 microspheres as scattering layer in dye-sensitized solar cells", *J. Mater. Sci. Mater. Electron.*, **29** (2018) 7356–7363.
39. Q. Wang, J.E. Moser, M. Grätzel, "Electrochemical impedance spectroscopic analysis of dye-sensitized solar cells", *J. Phys. Chem. B*, **31** (2005) 14945–14953.
40. H. Yu, S. Zhang, H. Zhao, G. Will, P. Liu, "An efficient and low-cost TiO_2 compact layer for performance improvement of dye-sensitized solar cells", *Electrochim. Acta*, **54** (2009) 1319–1324.
41. H. Xu, X. Tao, D.-T. Wang, Y.-Z. Zheng, J.-F. Chen, "Enhanced efficiency in dye-sensitized solar cells based on TiO_2 nanocrystal/nanotube double-layered films", *Electrochim. Acta*, **55** (2010) 2280–2285.
42. Y.P. Lin, S.Y. Lin, Y.C. Lee, Y.W. Chen-Yang, "High surface area electrospun prickle-like hierarchical anatase TiO_2 nanofibers for dye-sensitized solar cell photoanodes", *J. Mater. Chem. A*, **1** (2013) 9875–9884.
43. J.H. Kim, T.Y. Kim, K.H. Park, J.W. Lee, "Electron lifetimes in hierarchically structured photoelectrodes biotemplated from butterfly wings for dye-sensitized solar cells", *Int. J. Electrochem. Sci.*, **10** (2015) 5513–5520.
44. Y. Zhang, J. Cai, Y. Ma, L. Qi, "Mesocrystalline TiO_2 nanosheet arrays with exposed 001 facets: Synthesis via topotactic transformation and applications in dye-sensitized solar cells", *Nano Res.*, **8** (2017) 2610–2625.